

RESEARCH ARTICLE | JANUARY 03 2023

High-resolution x-ray spectrometer for x-ray absorption fine structure spectroscopy

D. A. Chin ; P. M. Nilson ; D. Mastrosimone ; D. Guy; J. J. Ruby ; D. T. Bishel ; J. F. Seely ; F. Coppari ; Y. Ping ; J. R. Rygg ; G. W. Collins 



Rev. Sci. Instrum. 94, 013101 (2023)

<https://doi.org/10.1063/5.0125712>



View
Online



Export
Citation

CrossMark



MAD CITY LABS INC.
www.madcitylabs.com

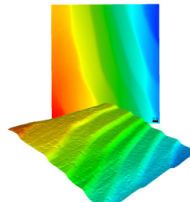
Nanopositioning Systems



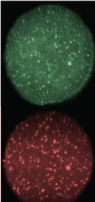
Modular Motion Control



AFM and NSOM Instruments



Single Molecule Microscopes



High-resolution x-ray spectrometer for x-ray absorption fine structure spectroscopy

Cite as: Rev. Sci. Instrum. 94, 013101 (2023); doi: 10.1063/5.0125712

Submitted: 13 September 2022 • Accepted: 4 December 2022 •

Published Online: 3 January 2023



View Online



Export Citation



CrossMark

D. A. Chin,^{1,2,a)} P. M. Nilson,² D. Mastrosimone,² D. Guy,² J. J. Ruby,³ D. T. Bishel,^{1,2} J. F. Seely,⁴ F. Coppari,³ Y. Ping,³ J. R. Rygg,^{1,2,5} and G. W. Collins^{1,2,5}

AFFILIATIONS

¹ Department of Physics and Astronomy, University of Rochester, Rochester, New York 14627, USA

² Laboratory for Laser Energetics, University of Rochester, Rochester, New York 14623-1299, USA

³ Lawrence Livermore National Laboratory, Livermore, California 94550, USA

⁴ Syntek Technologies, Fairfax, Virginia 22031, USA

⁵ Department of Mechanical Engineering, University of Rochester, Rochester, New York 14627, USA

^{a)} Author to whom correspondence should be addressed: dchin@lle.rochester.edu

ABSTRACT

Two extended x-ray absorption fine structure flat crystal x-ray spectrometers (EXFS's) were designed and built for high-resolution x-ray spectroscopy over a large energy range with flexible, on-shot energy dispersion calibration capabilities. The EXFS uses a flat silicon [111] crystal in the reflection geometry as the energy dispersive optic covering the energy range of 6.3–11.4 keV and achieving a spectral resolution of 4.5 eV with a source size of 50 μm at 7.2 keV. A shot-to-shot configurable calibration filter pack and Bayesian inference routine were used to constrain the energy dispersion relation to within ±3 eV. The EXFS was primarily designed for x-ray absorption fine structure (XAFS) spectroscopy and provides significant improvement to the Laboratory for Laser Energetics' OMEGA-60 XAFS experimental platform. The EXFS is capable of performing extended XAFS measurements of multiple absorption edges simultaneously on metal alloys and x-ray absorption near-edge spectroscopy to measure the electron structure of compressed 3d transition metals.

© 2023 Author(s). All article content, except where otherwise noted, is licensed under a Creative Commons Attribution (CC BY) license (<http://creativecommons.org/licenses/by/4.0/>). <https://doi.org/10.1063/5.0125712>

I. INTRODUCTION

Laser facilities, such as the Laboratory for Laser Energetics' (LLE's) OMEGA-60 laser,¹ are capable of compressing materials to above 100 GPa into the high-energy-density (HED) regime. At these extreme conditions, the behavior of matter fundamentally changes, leading to novel phenomena including complex crystallographic transitions,^{2,3} super-ionic states,^{4,5} electride phases,^{6,7} interspecies radiative transitions,⁸ and recently demonstrated electronic structural changes.^{9–11} A key challenge of characterizing materials at HED conditions, however, is determining the temperature of the compressed material.

X-ray absorption fine structure (XAFS) spectroscopy is a technique capable of providing insight into both the temperature and electronic structure of HED matter.^{12,13} XAFS spectroscopy is commonly split into two sections: extended x-ray absorption fine structure (EXAFS)^{14–17} spectroscopy and x-ray absorption near-edge spectroscopy (XANES).^{16,17} EXAFS spectroscopy uses

modulations above the absorption edge to characterize the local atomic structure and disorder from which temperature can be inferred.^{13,16,18} XANES encompasses the region around the absorption edge and can be used to constrain the electronic structure of the compressed material.^{19,20} Because XAFS is a transmission measurement with spectral modulations of the order of a few eV, high-throughput and high-resolving power x-ray spectrometers are required for single-shot measurements at large laser facilities.

The EXAFS flat crystal x-ray spectrometer (EXFS) was designed and built to improve the XAFS capabilities of OMEGA-60, allowing for electron structure and improved temperature measurements. Two spectrometers were constructed for XAFS measurements to provide two lines of sight to measure the incident spectrum (I_0) on the material of interest and the transmitted spectrum (I_t). Furthermore, a variable front-end filter pack and energy calibration routine constrain the energy dispersion of EXFS, which is critical for performing the XAFS spectroscopy. The energy dispersion directly impacts

the frequency of the EXAFS modulations and ultimately the density of the material.^{16,17} The filter pack also allows for small shifts in the absorption edge position of the order of a few eV to be measured, which can help identify the oxidation state of the absorbing atom.¹¹ Finally, by achieving a spectral resolution of a few eV, the EFX is capable of performing XANES measurements to understand the electron structure at HED conditions.

This manuscript outlines the design, characterization, and initial performance of EFX. Section II discusses the design of the spectrometer, Sec. III details the energy dispersion calibration of EFX, and Sec. IV describes the spectral resolution of EFX. Finally, the XAFS performance of EFX is shown in Sec. V.

II. SPECTROMETER DESIGN

A. Physical housing

Two EFX's were designed and built for OMEGA-60. The diagrams of the physical housing of EFX are shown in Fig. 1, where Fig. 1(a) highlights the different components of EFX and Fig. 1(b) shows a picture of EFX. The primary components of the spectrometer are a flat silicon [111] crystal and flat image plate detector, which is loaded into EFX through the back of the housing, opposite the x-ray source. The crystal and detector are held in an aluminum housing with an entrance port for the x rays on one side, as shown in Fig. 1(a). Four crystals were built for EFX: three 170 mm long Si [111] crystals and one 110 mm long Si [111] crystal. A blast shield to protect the crystal and a filter pack to characterize the energy dispersion are held in the front of EFX. To reduce noise, the EFX has a 3.175 mm-thick external tungsten shell and a 12.7 mm-thick tungsten line-of-sight block that protect the detector from the x-ray source. Furthermore, 150 μm of copper, 150 μm of stainless steel, 500 μm of aluminum, and 750 μm of polyethylene were layered at the bottom of the housing and the detector side of the line-of-sight

block to reduce internal fluorescence.²¹ This additional shielding helps reduce the background signal of EFX.

The relevant dimensions for the energy dispersion relation calculations of EFX are shown in Fig. 1(c). The central axis corresponds to the axis that runs through the x-ray source and the center of the detector. The minimum distance between the central axis and the center of the crystal is 65 mm, while the length of the crystal is 170 mm. The standoff distance between the crystal and the x-ray source, along the central axis, is 193.4 mm. The energy dispersion relation can be calculated from these dimensions and is discussed in Secs. II E and III.

B. Crystal

Three identical primary EFX crystals were constructed, which are flat $10 \times 170 \times 2 \text{ mm}^3$ silicon crystals cut along the [111] plane and cover the energy range of 6.3–11.4 keV. The longest dimension of the crystal was chosen to cover a large energy range and allow for XAFS measurements of the 3d transition metals between Mn and Zn as well as the ability to include multiple energy calibration features. Si [111] was chosen for its narrower rocking curve, allowing for a high spectral resolution. The crystal was optically contacted (held together by intermolecular forces) to a $15 \times 172 \times 4 \text{ mm}^3$ Pyrex® base so that the [111] plane was within ± 30 arc sec of the surface. The Pyrex base had a surface finish of $< 5 \text{ nm}$ and a flatness of five waves at 633 nm. The Pyrex base was chosen to match the coefficient of thermal expansion of the silicon crystal. To reduce the stress on the crystal, the crystal and Pyrex base were mounted to an aluminum substrate using set screws through the sides of the aluminum substrate that pinched the sides of the Pyrex base at a torque of 8.5 N cm, as shown in the cross section in Fig. 2. The EFX also has a smaller secondary silicon [111] crystal that is 110 mm long and covers the energy range of 6.4–9.2 keV. The data shown in this manuscript were measured with this 110 mm crystal as it was used as a proof of concept for the spectrometer.

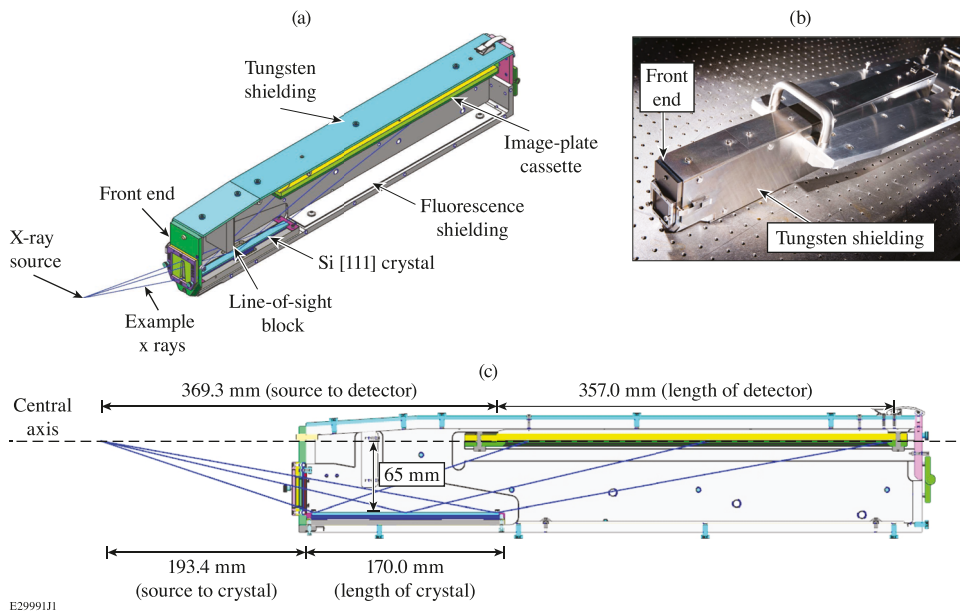


FIG. 1. (a) Schematic of EFX showing the positions of the Si [111] crystal (Sec. II B), the front end (Sec. II C), and the image-plate detector (Sec. II D). (b) Picture of the EFX. (c) Cross section of EFX highlighting the relevant distances for energy dispersion calculations (Secs. II E and III).

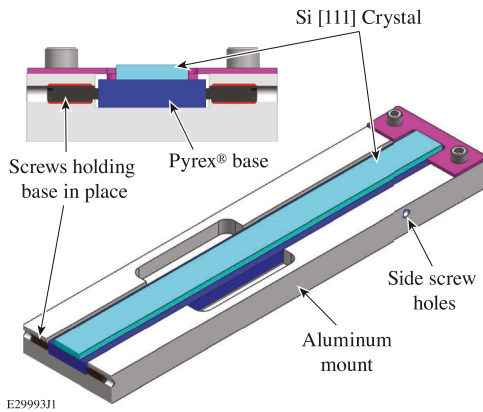


FIG. 2. EFX crystal and mounting assembly. The silicon [111] crystal is optically contacted (held together by intermolecular forces) to a Pyrex base. The Pyrex base is held to an aluminum mount with four side screws, two pairs toward either end of the base. The screws are highlighted in the cross-sectional image.

The integrated reflectivity of the 110 mm crystal was measured at an external x-ray calibration facility. The x rays were generated from a 30 kV electron source incident on a nickel foil. A calibrated Amptek silicon drift detector (SSD) was used to calibrate the x-ray emission from the nickel foil. The integrated reflectivity was measured at the nickel K_{α} energy (~ 7.5 keV) to be $\mathcal{R} = 0.035 \pm 0.014$ mrad. The uncertainty is dominated by the image-plate conversion. Future measurements are planned to reduce this uncertainty and measure the energy dependence of the integrated reflectivity along the length of the crystal. The 170 mm crystals are expected to have similar integrated reflectivities, which will also be measured in the future.

C. Front end

The front end of EFX was designed to protect the silicon crystal while allowing for flexible energy dispersion calibration and is made up of three primary parts, as shown in Fig. 3(a). First, the blast shield assembly protects the crystal from laser-driven target debris. The blast shield assembly primarily consists of a 254 μm of beryllium blast shield and a 6.35 mm-thick tungsten aperture, which limits the x rays to only those that illuminate the crystal. There is a smaller crystal aperture that can be used for the 110 mm crystal. An aluminum cover plate is placed over the front aperture to prevent damage to the beryllium when the spectrometer is not in use. Second, the front shield holds both the blast shield assembly and filter assembly to the main EFX body. Third, a filter assembly can hold adjustable filter packs for energy calibration and is shown in an expanded view in Fig. 3(b). The adjustable filter pack has distance markings along it to indicate the distance to the central axis of the spectrometer. These markings correspond to energies between 6.3 and 11.4 keV, allowing horizontal filters to be placed so that the filter's absorption edge will be in the correct energy range. Vertical filters can also be placed to cover one half of the spectrum in the non-dispersive direction.

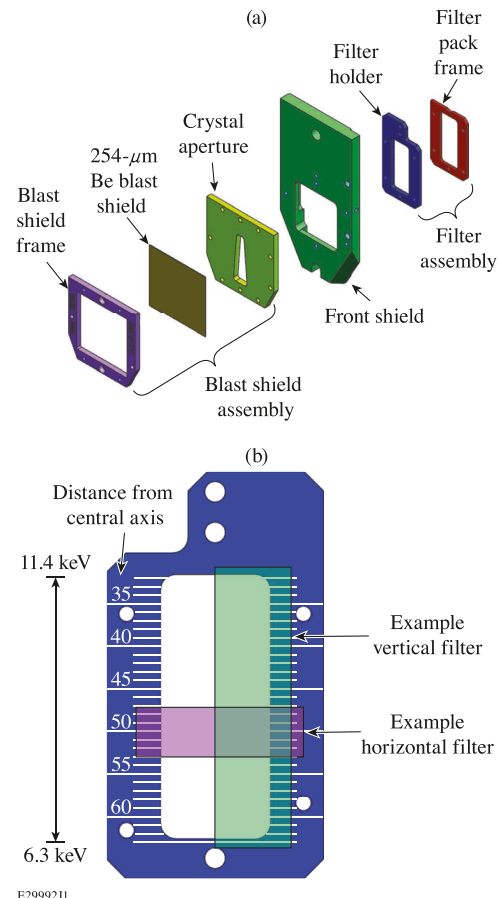


FIG. 3. (a) The EFX aperture consists of three primary components: a blast shield assembly, a front shield, and a filter assembly. (b) Calibration filters are held in the filter assembly and can be placed horizontally to cover specific energy ranges or vertically to cover the entire energy range but only part of the crystal.

D. Detector

The EFX uses a biological analysis system-multipurpose standard (BAS-MS) or biological analysis system-super resolution (BAS-SR) image plate as the primary detector. The image plate is $355.6 \times 28.58 \text{ mm}^2$ and is held in a lighttight cassette covered with 25.4 μm -thick black Kapton®. The image plate is scanned using a Typhoon fluorescence and laser (FLA) 7000 scanner, which outputs the counts in each pixel as a GEL file. The GEL data can be converted to photostimulated luminescence (PSL) using^{22,23}

$$\text{PSL} = \left(\frac{\text{GEL}}{2^b - 1} \right)^2 \left(\frac{r}{100} \right)^2 \left(\frac{4000}{s} \right) 10^{\ell/2}, \quad (1)$$

where $b = 16$ is the bit depth, r is the resolution in μm , s is the sensitivity, and ℓ is the scanner dynamic range latitude.²³ For EFX, the nominal scan settings are $r = 50 \mu\text{m}$, $s = 4000$, and $\ell = 5$. The PSL values can then be converted to photons²⁴ with a correction for the angle of incidence.²⁵

E. Design dispersion model

The design of the spectrometer was done using a simplified dispersion model in 2D with a flat crystal and flat detector, as shown in Fig. 4(a), where the crystal and detector are parallel ($D_y = 0$ and $\theta_D = 0$) and the x-ray source sits on the same line as the detector. The crystal and detector are separated by a distance $R = 65$ mm. In this geometry, the energy of an x ray (E) can be related to the position the x ray hits the detector (x),

$$E(x) = \frac{nhc}{2R} \frac{\sqrt{4R^2 + x^2}}{2d}, \quad (2)$$

where n is the reflection order ($n = 1$ for EFX), h is Planck's constant, c is the speed of light, and d is the spacing of the crystal planes, where $2d = 6.271$ Å for Si [111].²⁶ Figure 4(b) shows the change in energy per unit distance (dE/dx) and the energy as functions of the position on the detector assuming that the 6.2 keV x rays correspond to 0 mm on the detector and $D_x = 386.8$ mm.

F. Spectrometer sensitivity

To characterize the signal throughput of the spectrometer, we define the spectrometer sensitivity $G(E)$ in units of eV sr/pixel (or, often, eV sr/mm²) to be^{27–29}

$$G(E) = \frac{d\Omega}{dA} \frac{dE}{d\theta} \mathcal{R}(E), \quad (3)$$

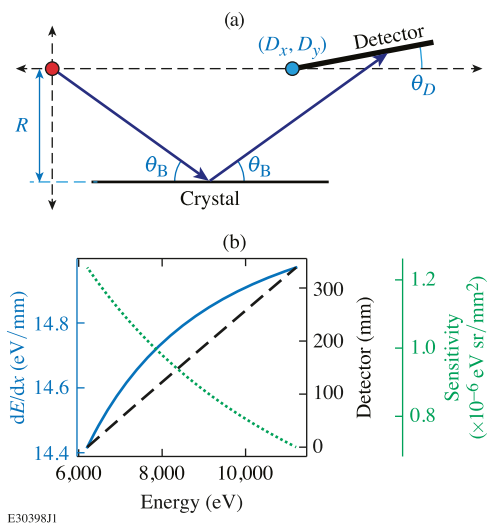


FIG. 4. (a) A 2D geometric model of EFX, where the coordinate system is chosen so that the x-ray source is at the origin and the crystal is parallel to the x axis. R represents the y offset of the crystal. D_x and D_y represent the x and y origins of the detector, and θ_D is the angle of the detector relative to the x axis. The detector and crystal are nominally separated by $R = 65$ mm. An example x ray (dark blue arrow) is shown reflecting off the crystal at the Bragg angle (θ_B) and hitting the detector. (b) The spectrometer energy dispersion, where the black dashed line represents the position of the incident x ray on the detector as a function of energy assuming $D_y = 0$, $\theta_D = 0$, and $D_x = 386.8$ mm. The blue line shows the change in energy per unit distance as a function of energy in eV/mm. The green dotted line is the sensitivity of EFX.

where $\frac{d\Omega}{dA}$ is the solid angle per area, $\frac{dE}{d\theta}$ is the spectrometer dispersion, and $\mathcal{R}(E)$ is the crystal integrated reflectivity, which was measured as discussed in Sec. II B at 7.5 keV and assumed constant. The analytical form for the solid angle per pixel along the central axis of EFX is given by

$$\frac{d\Omega}{dA}(E) = \int_{x(E)}^{x(E)+\ell_{IP}} \frac{2R\ell_{IP}}{(x^2 + 4R^2)^{3/2}} dx, \quad (4)$$

where $x(E)$ is given by Eq. (2), ℓ_{IP} is the size of the pixel, and R is the distance between the crystal and the central axis. The variation of the solid angle along the non-dispersive direction is below 1% and is, therefore, ignored in the calculation. Furthermore, the analytical form of $\frac{dE}{d\theta}$ is given as a function of the Bragg angle,

$$\theta_B = \sin^{-1}\left(\frac{nhc}{2dE}\right), \quad (5)$$

to be^{21,29}

$$\frac{dE}{d\theta}(E) = -E \cot(\theta_B). \quad (6)$$

The absolute value of $\frac{dE}{d\theta}$ is taken to ensure a positive sensitivity. The sensitivity of EFX as a function of energy for the central row of pixels is shown in Fig. 4(b).

The spectrometer sensitivity can be related to a source spectrum (S) in units of photons/eV/sr, where^{28,29}

$$S = \frac{D/S_{IP}(E)}{G(E)T(E)}, \quad (7)$$

in which D is the measured data in PSL/pixel, S_{IP} represents the image-plate sensitivity in units of PSL/photon,^{23,24} and $T(E)$ is the filter transmission.

III. ENERGY DISPERSION CALIBRATION

Although the simple dispersion model, as discussed in Sec. II E, was used to design EFX, a more sophisticated 2D model was used to perform the final energy calibration. This model has four free parameters (R , D_x , D_y , and θ_D), which are described in Fig. 4(a). Solving for the position on the detector (x_D) as a function of the Bragg angle,

$$x_D(\theta_B; R, D_x, D_y, \theta_D) = \sqrt{\frac{[(D_y + 2R) \cos(\theta_B) - D_x \sin(\theta_B)]^2}{\sin(\theta_B - \theta_D)^2}}. \quad (8)$$

In this dispersion model, $x_D = 0$ corresponds to the starting pixel of the data on the detector.

To constrain these four free parameters for a given shot and calibrate our data, we used cold K-edge filters placed horizontally in the filter assembly, as shown in Fig. 3(b). Due to the resolution of EFX, we were not able to assign a specific point in the absorption edge to a given energy.³⁰ Therefore, for each K-edge material, we built a transmission model based off the measured synchrotron data of the corresponding element.^{31,32} The measured synchrotron absorption coefficient [$\mu(E)$] for the given edge was converted to the transmitted signal (I_t) through the calibration foil measured with EFX,

$$I_t(E;t) = I_0(E)e^{-\mu(E)t}, \quad (9)$$

where I_0 is the incident signal on EFX (from a previous measurement) and t is the foil thickness that was left as a free parameter. This transmitted signal was then degraded using the EFX spectral response (discussed in Sec. IV) given a CH shell implosion x-ray source.³³ Finally, the transmitted signal was normalized using a signal multiplier and adjusted with a constant background term so that the model for each edge had three free parameters: the foil thickness (t), the maximum signal, and a constant background term.

We used a Bayesian inference routine^{34,35} and a Gaussian likelihood function to infer the four geometric parameters along with the free parameters in the transmission spectrum for each calibration edge. The data uncertainty was assumed to be the standard deviation in each column of pixels. Due to the multistage process of recording data on the image plate^{23,36} and the additional noise added by image plate scanners,^{37,38} Poisson photon counting statistics underestimates the uncertainty on the data. Because our model does not take into account signal correlations between pixels, a model for the data uncertainty was chosen that is an upper bound on the uncertainty in the mean signal for a column of pixels. A comparison of the Poisson counting with the standard deviation of the counts in a given column is shown in Fig. 5. To justify the choice of a Gaussian likelihood, a Gaussian function, whose sigma corresponds to the standard deviation of the signal level in the data column, is also overlaid in the figure as a solid gray line to demonstrate that the data roughly follow a Gaussian distribution. The identification of the true data uncertainty and corresponding likelihood function is beyond the scope of this paper.

To generate a starting set of priors for the geometric parameters, we analyzed a spectrum with five calibration edges, shown in Fig. 6. These data were taken on shot 100336 on OMEGA-60. The target was an 865 μm -outer-diameter (OD), 9 μm -thick CH shell, driven with 25 kJ of laser energy in a 1 ns square pulse.³³ Five energy calibration foils, 25 μm Mn, 4 μm Fe, 5 μm Co, 4 μm Ni, and 25 μm Cu, were placed horizontally in the filter pack.

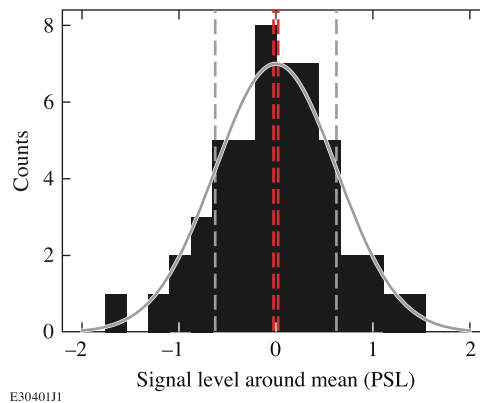


FIG. 5. The black histogram represents the signal of each pixel in a given column around the mean value for the center 50 rows. The dashed red lines are the error obtained with photon Poisson counting statistics, while the dashed gray lines represent the standard deviation of the signal level in the data column. Due to the multistage process of scanning image plate,^{23,36,37} Poisson counting statistics underestimates the error on the data. A Gaussian function, whose sigma corresponds to the standard deviation of the signal level in the data column, is also overlaid in the figure as a solid gray line.

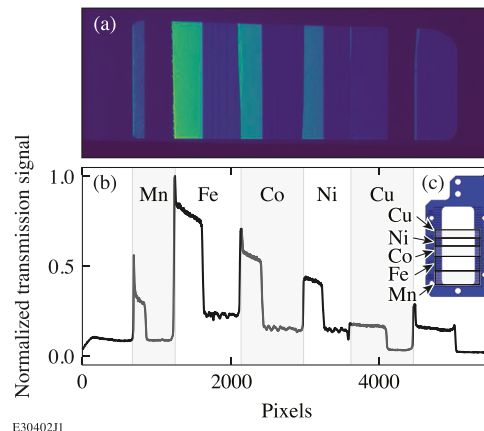


FIG. 6. Example EFX data taken on shot 100336 measured with the 110 mm Si [111] crystal. (a) The raw EFX spectrum with five different calibration foils, Mn, Fe, Co, Ni, and Cu, placed horizontally in the filter assembly. (b) The normalized lineout taken over the 50 central rows. The transmission spectrum shows the start of each foil along with the corresponding K-edge absorption roughly centered in each foil region and EXAFS modulations for the thinner foils (Fe, Co, and Ni). (c) Diagram of the filter pack showing the placement of the five different filters.

Figure 6(a) shows the raw data where the vertical strips represent the absorption K edges of each foil as well as the breaks between each filter. Figure 6(b) is a lineout of the central 50 rows of the spectrum. The posterior distributions of the geometric parameters from the inference were used as the starting set of priors for analyzing shots with less calibration edges. These values are shown in Table I.

To test this model, an example analysis of data with only Mn, Fe, and Cu calibration edges is shown in Fig. 7. The Mn and Cu K edges were used to infer the geometric parameters in the energy dispersion, and the validity of the inference was determined by a comparison to the Fe K edge, which was not included in the inference. Figure 7(a) shows the data in blue with a 1σ (68% credible interval) variation. The inset [Fig. 7(b)] shows the absorption coefficient model overlaid onto the data for the Cu edge, where the red band represents the model 1σ interval. Figure 7(c) shows the Fe K edge along with an example Fe transmission model edge to show that the calibration is consistent with the Fe K edge. A histogram of the energy distribution for a given pixel is shown in Fig. 7(d). The energy width of this distribution fluctuates depending upon the shot and the pixel chosen, but the standard deviation has an upper limit of ± 3 eV. Furthermore, this width is dependent upon the filters used in the

TABLE I. Posterior distributions of the four dispersion parameters obtained from analyzing five calibration edges. These inferred posterior distributions were used as prior distributions for other inferences.

Parameter	Mean	Standard deviation
R	62.6 mm	1.7 mm
D_x	379.7 mm	3.9 mm
D_y	-1.7 mm	3.5 mm
θ_D	0.0063 rad	0.0021 rad

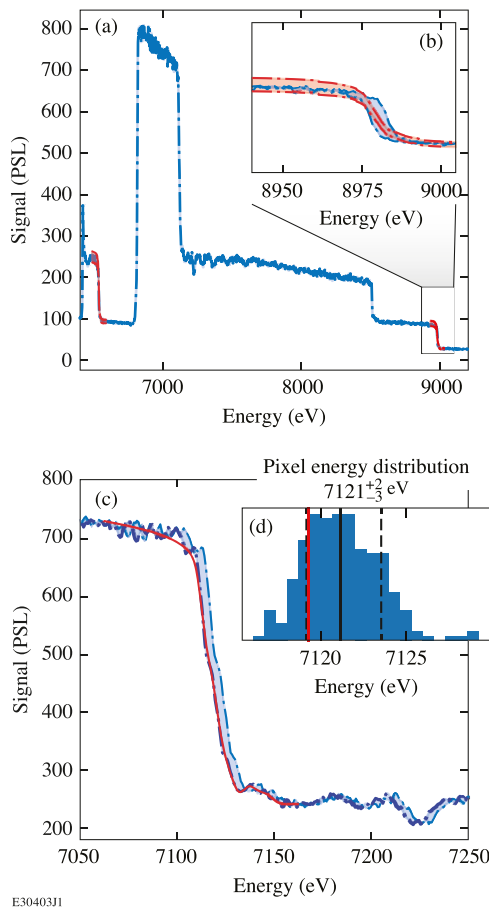


FIG. 7. (a) Energy calibration of shot 100347, where the Mn and Cu edges were used to perform the calibration. The blue region represents the 1σ (68% credible interval) data confidence interval, and the red region represents the 1σ transmission model confidence interval. (b) Expanded view of the Cu edge calibration highlighting the overlap between the data and the model. (c) The Fe edge that was not used during the calibration. The red line is an example overlaid transmission model for Fe showing that the calibration is consistent with the iron K edge. (d) Histogram of the energy values for a pixel on the Fe absorption edge, where the red vertical line corresponds to the transmission model shown in (c).

calibration. For example, if we calibrate to the Mn and Fe edges, the calibration has an uncertainty closer to ± 10 to 15 eV around the Cu edge due to the need to extrapolate the calibration. Finally, because of the shot day-to-shot day variability, the geometric priors shown in Table I should ideally be generated from analyzing the data taken on the same shot day as the experimental data.

There are a variety of ways to further improve this calibration model. First, additional terms can be added to the geometric model, such as allowing for curvature in the image plate; however, more calibration data would be required to constrain these additional parameters. Second, there is a slight energy dependence of the data in the non-dispersive direction most likely due to image plate curvature. This has no impact when taking narrow central lineouts but should be taken into account when averaging over the entire non-dispersive region. Finally, to measure small shifts in a small region

of energy, vertical filters can be placed over half of the front aperture, shown in Fig. 3(b). This allows for a constant calibration K edge in all shots, where small shifts can be measured locally relative to that edge to within ± 1 eV.

IV. SPECTRAL RESOLUTION

A. Theoretical model

Understanding the spectral resolution of EFX is critical for interpreting XANES and EXAFS data. Four terms were considered when modeling the spectral resolution of EFX: source size broadening, crystal rocking curve, detector resolution, and depth broadening due to x-ray penetration into the crystal. Each term was represented as a Gaussian whose full width at half maximum (FWHM) corresponded to

$$\text{Source:}^{29} \quad \delta E_{\text{source}} = \frac{dE}{dx} \frac{\delta_a}{\cos(\pi/2 - \alpha)}, \quad (10)$$

$$\text{Rocking curve:}^{29} \quad \delta E_{\text{rock}} = E \frac{\delta_{\text{rock}}}{\tan(\theta_B)}, \quad (11)$$

$$\text{Detector:}^{29} \quad \delta E_{\text{detector}} = \frac{dE}{dx} \delta_{\text{IP}}, \quad (12)$$

$$\text{Depth broadening:}^{39} \quad \delta E_{\text{depth}} = \frac{dE}{dx} 2\delta_D \cos(\theta_B), \quad (13)$$

where $\frac{dE}{dx}$ corresponds to the change in energy per unit distance along the detector and can be calculated from Eq. (2), δ_a is the source size in the detector plane, α is the angle between the x ray and the detector [the Bragg angle (θ_B) for EFX in the design geometry], $\delta_{\text{rock}} = 24$ arc sec is the rocking curve measured by the crystal manufacturers at the copper K α (8.04 keV), $\delta_{\text{IP}} = 0.1$ mm is the image-plate resolution,^{29,40} and δ_D is the x-ray penetration into the crystal, which was assumed to be the attenuation length in silicon as a function of x-ray energy.²⁶ The total spectral resolution can be estimated by convolving each of the individual Gaussian contributions together, which results in a Gaussian whose FWHM is obtained by adding all terms in quadrature,

$$\delta E_{\text{total}} = \sqrt{\delta E_{\text{source}}^2 + \delta E_{\text{rock}}^2 + \delta E_{\text{detector}}^2 + \delta E_{\text{depth}}^2}. \quad (14)$$

The spectral resolution for each term along with the total spectral resolution is shown in Fig. 8(a) as a function of energy, assuming a $50\text{ }\mu\text{m}$ source size. The spectral resolution for the Rowland-Yaakobi x-ray spectrometer (XRS),²⁹ previously used for XAFS measurements on OMEGA,^{12,13} is also shown for reference. Because flat crystals have such a strong dependence on source size, the total spectral resolution and the source size dependence are shown in Fig. 8(b) as a function of source size. The EFX is primarily dominated by source size broadening, especially with sources larger than 0.2 mm sources. Vacuum CH shell implosion x-ray sources, which are common XAFS x-ray sources on OMEGA-60,^{13,41} emit x rays in three different phases: corona ($850\text{ }\mu\text{m}$), core stagnation ($50\text{ }\mu\text{m}$), and afterglow ($300\text{ }\mu\text{m}$), where each phase can be associated with a different diameter sphere.³³ Figure 8(a) is shown assuming a $50\text{ }\mu\text{m}$ source size because the core stagnation accounts for $\sim 76\%$ of

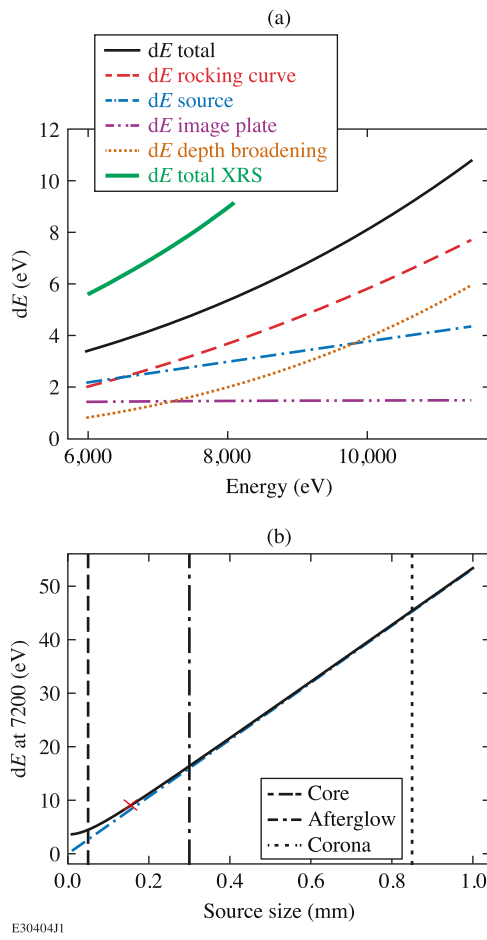


FIG. 8. (a) Spectral resolution for each term along with the total resolution in black. The source curve was generated assuming a source size of 50 μm . The spectral resolution for XRS (the previous OMEGA-60 XAFS spectrometer¹³) is also shown in green, assuming a Ge [111] crystal in the second position with a rocking curve calculated from the x-ray oriented programs (XOP)⁴² at 7.5 keV. (b) The spectral resolution from source size broadening (blue) and the total spectral resolution (black) as a function of source size at 7200 eV. The vertical dashed lines represent the three different x-ray source sizes for a CH shell implosion x-ray source, which is a common x-ray source for XAFS measurements on OMEGA-60.³³ The red \times represents the measured resolution as discussed in Sec. IV B.

the x-ray emission.³³ Vertical dashed lines in Fig. 8(b) indicate the diameters of each of these phases and the corresponding EFX resolution of 45.4, 4.5, and 16.4 eV for the corona, core, and afterglow, respectively, at 7.2 keV.

B. Experimental verification

The spectral resolution model was initially verified on cold K_{α} emission. As discussed in Sec. II B, the nickel K_{α} emission was measured from an external source using the 110 mm Si [111] crystal and the measured spectrum is shown in Fig. 9. The source was measured with a pinhole camera to be roughly Gaussian with a FWHM of 150 μm . The intrinsic linewidth of the K_{α} emission, assumed to be a sum of Lorentzian distributions,⁴³ was convolved with a Gaussian

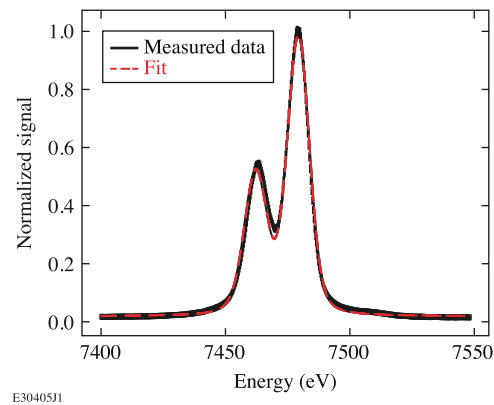


FIG. 9. Measured Ni K_{α} emission in black along with the fit to extract the spectral resolution of EFX in red. The spectral resolution of EFX was inferred to be 9.1 eV from the fit.

of a variable FWHM meant to represent the EFX spectral resolution. This degraded K_{α} emission was compared with the data, and a Bayesian inference routine^{35,44,45} was used to determine the optimal FWHM, and ultimately the spectral resolution at ~ 7.5 keV, to be 9.1 eV. This result is plotted as a red \times shown in Fig. 8(b) and agrees well with the theoretical resolution model.

The spectral resolution model was also verified on OMEGA-60 shots by comparing the measured EXAFS spectrum to a simulated one. A 4 μm iron filter was placed in the EFX filter pack, similar to Fig. 6, to measure the transmission spectrum through iron (I_t). The x-ray source was an implosion CH capsule driven with 24 kJ at a 1 ns square pulse.³³ The transmission spectrum was converted to the absorption coefficient (μ) using Eq. (9) and an I_0 measured on a

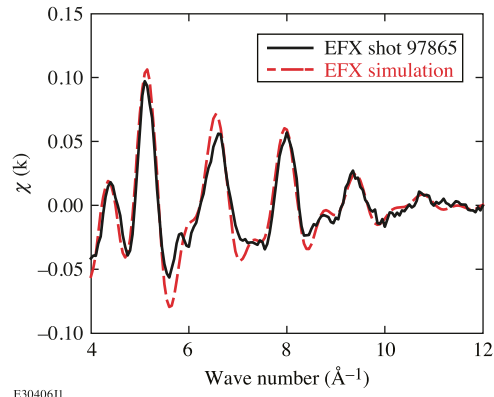


FIG. 10. EFX data were taken with a 4 μm -thick iron foil in the front end of EFX on shot 97865, and the EXAFS data (black solid line) were extracted as $\chi(k)$. The EXAFS data were also simulated using FEFF and degraded with the EFX spectral resolution for the given x-ray source (red dashed line). The simulated EXAFS data are in good agreement with the measured data, indicating that the spectral resolution model is capturing the correct behavior of EFX.

previous shot. The absorption coefficient was then converted to the EXAFS modulations (χ),¹⁶

$$\chi(k) = \frac{\mu - \mu_0}{\mu_0}, \quad (15)$$

where μ_0 is the absorption coefficient without neighboring atoms and $k = \sqrt{\frac{2m_e}{\hbar^2}(E - E_0)}$, in which \hbar is Planck's constant divided by 2π , m_e is the electron mass, and E_0 is the energy of the absorption edge. The resulting EXAFS modulations χ are shown in Fig. 10.

To simulate the EXAFS modulations, a theoretical absorption spectrum was produced using FEFF⁴⁶ assuming an amplitude reduction factor (S_0^2) of 0.8, a temperature of 300 K, and a Debye temperature of 420 K (Ref. 47). Using the measured I_0 , the absorption coefficient was converted into a simulated transmission

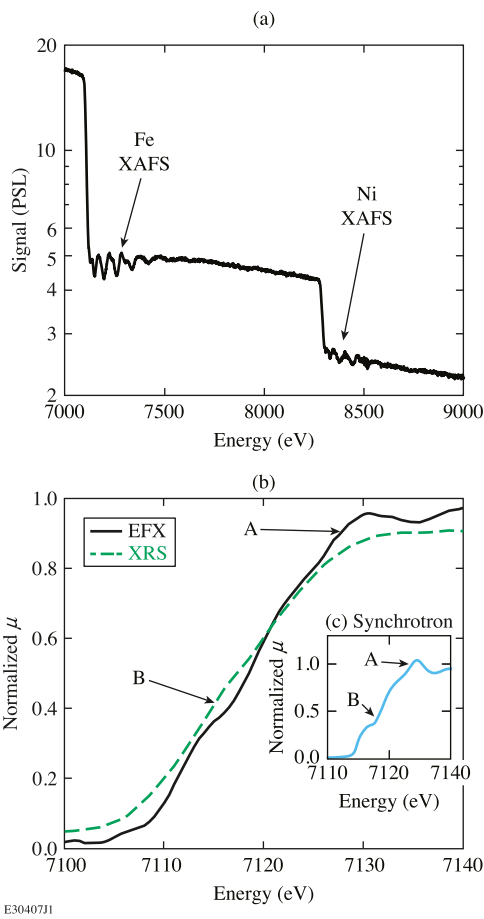


FIG. 11. (a) Measured EXAFS spectra from Invar ($\text{Fe}_{64}\text{Ni}_{36}$) showing the Fe and Ni K edges from shot 100646. The figure demonstrates the large energy range and capability of EFX to perform EXAFS on multiple edges of the same alloy simultaneously. (b) Comparison of iron XANES data between an EFX spectrum (black solid line) and an XRS spectrum (green dashed line), both taken on shot 97178. The higher resolution of EFX allows it to capture more details in the white line (point A) and the central modulation (point B). (c) An iron synchrotron spectrum,³¹ where the same A and B points are highlighted similar to (b).

measurement. This theoretical spectrum was then degraded with three Gaussians whose FWHM and individual weights correspond to the three different sources commonly found in XAFS backscatterers as discussed in Ref. 33. The simulated spectra agree well with the measured spectrum as shown in Fig. 10.

V. PERFORMANCE

The performance of EFX was tested on OMEGA-60 by simultaneously measuring EXAFS from multiple K edges of an alloy material. Invar ($\text{Fe}_{64}\text{Ni}_{36}$) foil was placed in the front-end filter pack of EFX, and the EXAFS spectrum from the Fe and Ni K edges was measured. The resulting spectra are shown in Fig. 11(a). By measuring two edges simultaneously, we are able to analyze both the iron and nickel K edges, allowing for more information to be extracted from a single shot.

The improved spectral resolution of EFX allows for XANES measurements to be made on OMEGA-60. Figure 11(b) shows the XANES from an iron foil in the front end of EFX from an 860 μm OD, 9 μm -thick CH implosion x-ray source driven with 18 kJ (Ref. 33). The transmission spectrum was converted into the

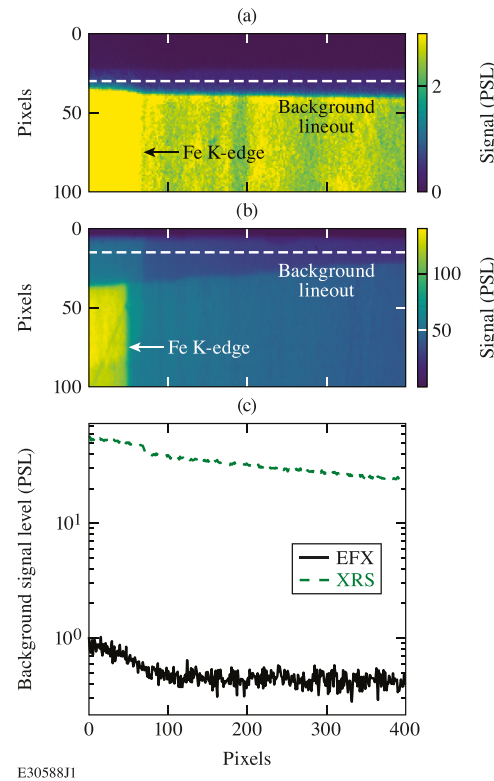


FIG. 12. (a) EFX and (b) XRS spectra where the raw data are shown around the Fe K-edge. A lineout of the background was taken along the dashed white line, and the comparison is shown in (c), where the EFX background level is the black solid line and the XRS background level is the dashed green line. The background signal level of EFX is improved by a factor of $\sim 70\times$ relative to XRS due to the improved shielding of EFX.

absorption coefficient using a previously measured I_0 . A spectrum measured by XRS on the same shot is also shown for reference. XRS has previously been used to measure EXAFS on OMEGA-60^{13,41} but was not able to perform XANES measurements. To highlight the key XANES features, the spectrum from iron measured at a synchrotron³¹ is shown in Fig. 11(c). The improved resolution of EFX is shown in the spectrum's steeper slope and the ability to begin to capture the white line (point A) and central modulation (point B), which can be used to distinguish structural changes and melting in iron.⁴⁸ XANES pre-edge features have also been shown to increase with increasing compression,¹⁰ meaning that these features may become more apparent during laser-driven experiments. This improved resolution in the XANES region of the spectrum will allow for future electron structure measurements of compressed materials, such as electron temperature^{49,50} and electron transitions.¹⁰

The additional shielding discussed in Sec. II A significantly reduced the background level of EFX relative to XRS. Figures 12(a) and 12(b) shows a comparison of the spectra around the iron K-edge of EFX and XRS taken on shot 97178. The background level is estimated by taking single row lineouts from regions not illuminated by the crystal (noted by the dashed white lines). The background level for each spectrometer is shown in Fig. 12(c). The absolute background level of EFX is improved by a factor of $\sim 70\times$ compared to XRS. The ratio of signal to background level in EFX is around $\sim 4\times$ greater for EFX than for XRS.

VI. CONCLUSIONS

We have built and characterized the EFX x-ray spectrometer to improve XAFS experimental capabilities on the LLE's OMEGA-60 Laser System. The EFX is a flat silicon [111] crystal spectrometer with two crystals, where the larger 170 mm crystal covers 6.3–11.4 keV and the smaller 110 mm crystal was used to characterize the performance of EFX. The two EFX's can be deployed for each shot granting two lines of sight and the ability to simultaneously measure I_0 and I_t . Furthermore, front-end filter packs and a Bayesian inference edge fitting routine allow for the energy dispersion relation to be constrained to within ± 3 eV and vertical filters can be used to constrain the energy dispersion even further. Finally, the EFX has a spectral resolution of 4.5 eV with a source size of 50 μm at 7.2 keV that has been benchmarked on external x-ray sources and on experimental OMEGA-60 shots. This increased spectral resolution will allow for XANES measurements on OMEGA-60 to characterize the changes in the electron structure that occur at HED conditions. In conclusion, the EFX has many applications on OMEGA-60 beyond XAFS, including x-ray emission and absorption spectroscopy of many 3d transition metals or monitoring x-ray sources used in x-ray diffraction and x-ray radiography experiments.

ACKNOWLEDGMENTS

The authors thank M. Shoup, A. Agliata, R. Jungquist, and D. Weiner for discussion and feedback on the spectrometer design and fabrication. This material is based upon the work supported by the Department of Energy National Nuclear Security Administration under Award No. DE-NA0003856, the University of Rochester, and the New York State Energy Research and Development Authority. The support of the DOE does not constitute an endorsement by

the DOE of the views expressed in this paper. D.A.C. acknowledges the DOE NNSA SSGF support, which is provided under Cooperative Agreement No. DE-NA0003960. This collaborative work was partially supported under the auspices of the U.S. Department of Energy by Lawrence Livermore National Laboratory under Contract No. DE-AC52-07NA27344.

This report was prepared as an account of the work sponsored by an agency of the U.S. Government. Neither the U.S. Government nor any agency thereof, nor any of their employees, makes any warranty, express or implied, or assumes any legal liability or responsibility for the accuracy, completeness, or usefulness of any information, apparatus, product, or process disclosed, or represents that its use would not infringe privately owned rights. Reference herein to any specific commercial product, process, or service by trade name, trademark, manufacturer, or otherwise does not necessarily constitute or imply its endorsement, recommendation, or favoring by the U.S. Government or any agency thereof. The views and opinions of the authors expressed herein do not necessarily state or reflect those of the U.S. Government or any agency thereof.

AUTHOR DECLARATIONS

Conflict of Interest

The authors have no conflicts to disclose.

Author Contributions

D. A. Chin: Conceptualization (equal); Data curation (equal); Formal analysis (lead); Investigation (equal); Methodology (equal); Project administration (equal); Resources (supporting); Software (equal); Validation (equal); Visualization (lead); Writing – original draft (lead). **P. M. Nilson:** Conceptualization (equal); Data curation (equal); Formal analysis (supporting); Funding acquisition (lead); Investigation (equal); Methodology (equal); Project administration (equal); Resources (supporting); Software (supporting); Supervision (equal); Validation (supporting); Visualization (supporting); Writing – review & editing (equal). **D. Mastrosimone:** Investigation (supporting); Methodology (equal); Project administration (equal); Resources (lead); Software (supporting); Supervision (equal); Validation (supporting). **D. Guy:** Formal analysis (supporting); Investigation (supporting); Methodology (equal); Project administration (equal); Resources (supporting); Software (equal); Validation (supporting); Visualization (supporting). **J. J. Ruby:** Data curation (supporting); Formal analysis (supporting); Investigation (supporting); Methodology (supporting); Software (supporting); Validation (supporting); Visualization (supporting); Writing – review & editing (equal). **D. T. Bishel:** Data curation (supporting); Formal analysis (supporting); Investigation (supporting); Methodology (supporting); Software (supporting); Validation (supporting); Visualization (supporting); Writing – review & editing (equal). **J. F. Seely:** Validation (equal); Writing – review & editing (equal). **F. Coppari:** Conceptualization (supporting); Investigation (supporting); Methodology (supporting); Writing – review & editing (equal). **Y. Ping:** Conceptualization (supporting); Investigation (supporting); Methodology (supporting). **J. R. Rygg:** Conceptualization (supporting); Funding acquisition (supporting); Investigation (supporting); Methodology (supporting); Project administration

(supporting); Software (supporting); Supervision (equal); Validation (supporting); Visualization (supporting); Writing – review & editing (equal). **G. W. Collins:** Conceptualization (supporting); Funding acquisition (supporting); Investigation (supporting); Methodology (supporting); Project administration (supporting); Software (supporting); Supervision (equal); Validation (supporting); Visualization (supporting); Writing – review & editing (equal).

DATA AVAILABILITY

The data that support the findings of this study are available from the corresponding author upon reasonable request.

REFERENCES

- ¹T. R. Boehly, D. L. Brown, R. S. Craxton, R. L. Keck, J. P. Knauer, J. H. Kelly, T. J. Kessler, S. A. Kumpan, S. J. Loucks, S. A. Letzring, F. J. Marshall, R. L. McCrory, S. F. B. Morse, W. Seka, J. M. Soures, and C. P. Verdon, *Opt. Commun.* **133**, 495 (1997).
- ²D. N. Polsin, D. E. Fratanduono, J. R. Rygg, A. Lazicki, R. F. Smith, J. H. Eggert, M. C. Gregor, B. H. Henderson, J. A. Delettrez, R. G. Kraus, P. M. Celliers, F. Coppapi, D. C. Swift, C. A. McCoy, C. T. Seagle, J.-P. Davis, S. J. Burns, G. W. Collins, and T. R. Boehly, *Phys. Rev. Lett.* **119**, 175702 (2017); **120**, 029902 (2018).
- ³F. Coppapi, R. F. Smith, J. Wang, M. Millot, D. Kim, J. R. Rygg, S. Hamel, J. H. Eggert, and T. S. Duffy, *Nat. Geosci.* **14**, 121 (2021).
- ⁴M. Millot, S. Hamel, J. R. Rygg, P. M. Celliers, G. W. Collins, F. Coppapi, D. E. Fratanduono, R. Jeanloz, D. C. Swift, and J. H. Eggert, *Nat. Phys.* **14**, 297 (2018).
- ⁵M. Millot, F. Coppapi, J. R. Rygg, A. Correa Barrios, S. Hamel, D. C. Swift, and J. H. Eggert, *Nature* **569**, 251 (2019).
- ⁶R. Paul, S. X. Hu, V. V. Karasiev, S. A. Bonev, and D. N. Polsin, *Phys. Rev. B* **102**, 094103 (2020).
- ⁷D. N. Polsin, A. Lazicki, X. Gong, S. J. Burns, F. Coppapi, L. E. Hansen, B. J. Henderson, M. F. Huff, M. I. McMahon, M. Millot, R. Paul, R. F. Smith, J. H. Eggert, G. W. Collins, and J. R. Rygg, *Nat. Commun.* **13**, 2534 (2022).
- ⁸S. X. Hu, V. V. Karasiev, V. Recoules, P. M. Nilson, N. Brouwer, and M. Torrent, *Nat. Commun.* **11**, 1989 (2020).
- ⁹E. Bykova, L. Dubrovinsky, N. Dubrovinskaia, M. Bykov, C. McCammon, S. V. Ovsyannikov, H.-P. Liermann, I. Kupenko, A. I. Chumakov, R. Rüffer, M. Hanfland, and V. Prakapenka, *Nat. Commun.* **7**, 10661 (2016).
- ¹⁰A. Sanson, I. Kantor, V. Cerantola, T. Irifune, A. Carnera, and S. Pascarelli, *Phys. Rev. B* **94**, 014112 (2016).
- ¹¹E. Boulard, M. Harmand, F. Guyot, G. Lelong, G. Morard, D. Cabaret, S. Boccato, A. D. Rosa, R. Briggs, S. Pascarelli, and G. Fiquet, *Geophys. Res. Lett.* **46**, 1348, <https://doi.org/10.1029/2019gl081922> (2019).
- ¹²B. Yaakobi, T. R. Boehly, D. D. Meyerhofer, T. J. B. Collins, B. A. Remington, P. G. Allen, S. M. Pollaine, H. E. Lorenzana, and J. H. Eggert, *Phys. Rev. Lett.* **95**, 075501 (2005).
- ¹³Y. Ping, F. Coppapi, D. G. Hicks, B. Yaakobi, D. E. Fratanduono, S. Hamel, J. H. Eggert, J. R. Rygg, R. F. Smith, D. C. Swift, D. G. Braun, T. R. Boehly, and G. W. Collins, *Phys. Rev. Lett.* **111**, 065501 (2013).
- ¹⁴M. Newville, *Rev. Mineral. Geochem.* **78**, 33 (2014).
- ¹⁵J. J. Rehr and R. C. Albers, *Rev. Mod. Phys.* **72**, 621 (2000).
- ¹⁶G. Bunker, *Introduction to XAFS: A Practical Guide to X-Ray Absorption Fine Structure Spectroscopy* (Cambridge University Press, Cambridge, England, 2010).
- ¹⁷D. Koningsberger and R. Prins, *X-Ray Absorption: Principles, Applications, Techniques of EXAFS, SEXAFS, and XANES*, Chemical Analysis: A Series of Monographs on Analytical Chemistry and its Applications (John Wiley & Sons, 1988).
- ¹⁸E. Sevillano, H. Meuth, and J. J. Rehr, *Phys. Rev. B* **20**, 4908 (1979).
- ¹⁹J. J. Rehr and A. L. Ankudinov, *Coord. Chem. Rev.* **249**, 131 (2005).
- ²⁰F. Dorchies and V. Recoules, *Phys. Rep.* **657**, 1 (2016).
- ²¹L. C. Jarrott, M. S. Wei, C. McGuffey, F. N. Beg, P. M. Nilson, C. Sorce, C. Stoeckl, W. Theobald, H. Sawada, R. B. Stephens, P. K. Patel, H. S. McLean, O. L. Landen, S. H. Glenzer, and T. Döppner, *Rev. Sci. Instrum.* **88**, 043110 (2017).
- ²²G. J. Williams, B. R. Maddox, H. Chen, S. Kojima, and M. Millicchia, *Rev. Sci. Instrum.* **85**, 11E604 (2014).
- ²³M. J. Rosenberg, D. B. Thorn, N. Izumi, D. Williams, M. Rowland, G. Torres, M. Haugh, P. Hillyard, N. Adelman, T. Schuler, M. A. Barrios, J. P. Holder, M. B. Schneider, K. B. Fournier, D. K. Bradley, and S. P. Regan, *Rev. Sci. Instrum.* **90**, 013506 (2019); **90**, 029902 (2019).
- ²⁴T. Bonnet, M. Comet, D. Denis-Petit, F. Gobet, F. Hannachi, M. Tarisien, M. Versteegen, and M. M. Aléonard, *Rev. Sci. Instrum.* **84**, 103510 (2013).
- ²⁵J. R. Rygg, R. F. Smith, A. E. Lazicki, D. G. Braun, D. E. Fratanduono, R. G. Kraus, J. M. McNamey, D. C. Swift, C. E. Wehrenberg, F. Coppapi, M. F. Ahmed, M. A. Barrios, K. J. M. Blobaum, G. W. Collins, A. L. Cook, P. Di Nicola, E. G. Dzenitis, S. Gonzales, B. F. Heidl, M. Hohenberger, A. House, N. Izumi, D. H. Kalantar, S. F. Khan, T. R. Kohut, C. Kumar, N. D. Masters, D. N. Polsin, S. P. Regan, C. A. Smith, R. M. Vignes, M. A. Wall, J. Ward, J. S. Wark, T. L. Zobrist, A. Arsenlis, and J. H. Eggert, *Rev. Sci. Instrum.* **91**, 043902 (2020).
- ²⁶B. L. Henke, E. M. Gullikson, and J. C. Davis, *At. Data Nucl. Data Tables* **54**, 181 (1993).
- ²⁷R. E. Marrs, G. V. Brown, J. A. Emig, and R. F. Heeter, *Rev. Sci. Instrum.* **85**, 11D626 (2014).
- ²⁸F. Coppapi, D. B. Thorn, G. E. Kemp, R. S. Craxton, E. M. Garcia, Y. Ping, J. H. Eggert, and M. B. Schneider, *Rev. Sci. Instrum.* **88**, 083907 (2017).
- ²⁹D. B. Thorn, F. Coppapi, T. Döppner, M. J. MacDonald, S. P. Regan, and M. B. Schneider, *Rev. Sci. Instrum.* **89**, 10F119 (2018).
- ³⁰S. Kraft, J. Stümpel, P. Becker, and U. Kuetgens, *Rev. Sci. Instrum.* **67**, 681 (1996).
- ³¹International X-Ray Absorption Society, IXAS X-Ray Absorption Data Library; accessed September 30, 2020, <https://xaslib.xrayabsorption.org/elem/>.
- ³²Institute for Catalysis Hokkaido University, XAFS database; accessed November 09, 2020, <https://www.cat.hokudai.ac.jp/catdb/index.php?action=dbinp>.
- ³³D. A. Chin, J. J. Ruby, P. M. Nilson, D. T. Bishel, F. Coppapi, Y. Ping, A. L. Coleman, R. S. Craxton, J. R. Rygg, and G. W. Collins, *Phys. Plasmas* **29**, 052702 (2022).
- ³⁴J. Salvatier, T. V. Wiecki, and C. Fonnesbeck, *PeerJ Comput. Sci.* **2**, e55 (2016).
- ³⁵J. J. Ruby, J. R. Rygg, D. A. Chin, J. A. Gaffney, P. J. Adrian, D. Bishel, C. J. Forrest, V. Yu. Glebov, N. V. Kabadi, P. M. Nilson, Y. Ping, C. Stoeckl, and G. W. Collins, *Phys. Rev. E* **102**, 053210 (2020).
- ³⁶M. Stoeckl and A. A. Solodov, *Rev. Sci. Instrum.* **89**, 063101 (2018).
- ³⁷M. Ito and Y. Amemiya, *Nucl. Instrum. Methods Phys. Res., Sect. A* **310**, 369 (1991).
- ³⁸Y. Ping and F. Coppapi, *High Pressure Res.* **36**, 303 (2016).
- ³⁹G. E. Ice and C. J. Sparks, *Nucl. Instrum. Methods Phys. Res., Sect. A* **291**, 110 (1990).
- ⁴⁰G. Fiksel, F. J. Marshall, C. Mileham, and C. Stoeckl, *Rev. Sci. Instrum.* **83**, 086103 (2012).
- ⁴¹Y. Ping, D. G. Hicks, B. Yaakobi, F. Coppapi, J. Eggert, and G. W. Collins, *Rev. Sci. Instrum.* **84**, 123105 (2013).
- ⁴²M. Sánchez del Río and R. J. Dejus, *Proc. SPIE* **8141**, 814115 (2011).
- ⁴³G. Hölzer, M. Fritsch, M. Deutsch, J. Härtwig, and E. Förster, *Phys. Rev. A* **56**, 4554 (1997).
- ⁴⁴D. Phan, N. Pradhan, and M. Jankowiak, “Composable effects for flexible and accelerated probabilistic programming in NumPyro,” [arXiv:1912.11554](https://arxiv.org/abs/1912.11554) (2019).
- ⁴⁵E. Bingham, J. P. Chen, M. Jankowiak, F. Obermeyer, N. Pradhan, T. Karaletsos, R. Singh, P. A. Szerlip, P. Horsfall, and N. D. Goodman, *J. Mach. Learn. Res.* **20**(28), 1–6 (2019).
- ⁴⁶J. J. Rehr, J. J. Kas, F. D. Vila, M. P. Prange, and K. Jorissen, *Phys. Chem. Chem. Phys.* **12**, 5503 (2010).
- ⁴⁷N. W. Ashcroft and N. D. Mermin, *Solid State Physics*, 1st ed. (Brooks/Cole, Pacific Grove, CA, 1976).
- ⁴⁸M. Harmand, A. Ravasio, S. Mazevet, J. Bouchet, A. Denoed, F. Dorchies, Y. Feng, C. Fourment, E. Galtier, J. Gaudin, F. Guyot, R. Kodama, M. Koenig, H. J. Lee, K. Miyaniishi, G. Morard, R. Musella, B. Nagler, M. Nakatsutsumi, N. Ozaki,

V. Recoules, S. Toleikis, T. Vinci, U. Zastrau, D. Zhu, and A. Benuzzi-Mounaix, *Phys. Rev. B* **92**, 024108 (2015).

⁴⁹A. Lévy, F. Dorchies, M. Harmand, C. Fourment, S. Hulin, O. Peyrusse, J. J. Santos, P. Antici, P. Audebert, J. Fuchs, L. Lancia, A. Mancic, M. Nakatsutsumi,

S. Mazevet, V. Recoules, P. Renaudin, and S. Fourmaux, *Plasma Phys. Controlled Fusion* **51**, 124021 (2009).

⁵⁰N. Jourdain, V. Recoules, L. Lecherbourg, P. Renaudin, and F. Dorchies, *Phys. Rev. B* **101**, 125127 (2020).